Chapter 11

Drop Dynamics in Complex Fluids

James J. Feng

*Department of Chemical and Biological Engineering and
Department of Mathematics, University of British Columbia,
Vancouver, BC V6T 1Z3, Canada
jfeng@chbe.ubc.ca*

Xiaopeng Chen

*School of Mechanics, Civil Engineering and Architecture, Northwestern
Polytechnical University, Xi'an, Shaanxi, P. R. China 710072*

Pengtao Yue

*Department of Mathematics, Virginia Polytechnic Institute and State
University, Blacksburg, VA 24061-0123, USA*

Chunfeng Zhou

*Department of Chemical Engineering and Materials Science,
University of Minnesota, Minneapolis, MN 55455-0132, USA*

This chapter describes the unusual behavior of interfaces between complex fluids through two examples: the partial coalescence between a drop and a planar interface, and the interaction and self-assembly of droplets suspended in a nematic liquid crystal. The main message is that coupling among 3 disparate length scales — the microscopic scale of molecular and supramolecular configuration, the mesoscopic scale of the interfaces, and the macroscopic scale of hydrodynamics — produces interfacial dynamics that may differ markedly from that in Newtonian fluids. A diffuse-interface theory provides a convenient framework for describing two-phase complex fluids, and finite-element computations reproduce the main features of the experimental observations, and reveal the underlying physical mechanisms.

340   *Feng, Chen, Yue and Zhou*

1. Introduction

The terms complex fluids and soft matter seem to both refer to materials
with unusual mechanical behavior that are intermediate, in some sense,
between ordinary fluids and solids. Examples range from common house-
hold materials such as tooth paste and hair gel to micro-engineered high-
performance composite materials, from synthetic polymers to biological
tissues and blood. From a mechanical viewpoint, these materials are distin-
guished by a *microstructure* that evolves as a result of deformation, which
in return modifies the rheology of the material and thus its flow behavior.
For example, polymer solutions exhibit viscoelasticity, a combination of
viscosity and elasticity, and peculiar behavior such as rod-climbing.[1] The
elasticity stems from the polymer chains — the microstructure for polymer
solutions — being stretched and oriented by flow and deformation.

In technological applications, complex fluids are often used not in the
pure form, but in mixtures with another material. An example is polymer
blends made of two immiscible polymers which possess, ideally, desirable
properties of each of the components. Other examples of complex fluid
mixtures include thermoplastic foam and oil-water emulsions. The overall
rheology of such materials depends critically on the shape, size and ori-
entation of the interfaces between the components. With the advent of
micro-engineering and nano-technology, the characteristic length scale of
the processing flow becomes ever smaller. As a result, the interfaces exert
ever increasing influences on the overall properties of the mixture relative
to the bulk properties. This has motivated much of the recent research on
interfacial dynamics in complex fluids.

From a more fundamental point of view, such problems are intriguing
because the interfacial behavior of complex fluids can differ markedly from
that of Newtonian fluids. As an example, consider a thin filament of New-
tonian fluid such as water suspended in an oil bath or in air. Because of
surface tension, the thread will quickly break up into droplets of more or
less uniform radius. The process, known as the Rayleigh instability,[2] starts
with the appearance of capillary waves on the thread, which quickly grow
in amplitude and cause pinch-off at the nodes of the waveform. If the fila-
ment is a viscoelastic polymer solution, the appearance of capillary waves is
followed by thinning of the thread but not rapid breakup. Instead, smaller
beads form between the larger ones as the thread continues to thin. In the
end, several generations of beads coexist in a spectacular beads-on-a-string
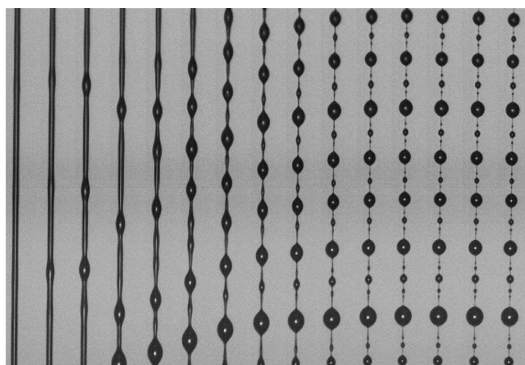morphology (Fig. 1), which persists for a long time before breakup.[3] The

Fig. 1.   Evolution of a thread of polymer solution (0.2% of poly(ethylene oxide) in ethylene glycol and water). The images of the thread represent advance in time from left to right, with neighboring images 25 ms apart. The initial filament diameter is approximately 40 μm. Adapted from Oliveira and McKinley[3] with permission, ©2005 American Institute of Physics.

longevity of the thread is due to the long polymer chains in the solution. The thinning of the thread stretches and aligns the chains, which drastically increases the filament's elongational viscosity, namely its resistance to further thinning and breakup.

As a second example, consider a drop of nematic liquid crystal suspended in an isotropic medium with matching density.[4] If the drop was an *isotropic* liquid such as water, naturally it would assume a spherical shape so as to minimize its surface area. The liquid crystal is made of elongated molecules that, in the nematic state, are more or less aligned with each other. The average orientation at any spatial point can be indicated by a unit vector called the director. Furthermore, they prefer to orient in a specific angle relative to the drop surface, a tendency commonly called anchoring. For the materials in this example, the anchoring is tangential to the interface. The drop then takes on an elongated lemon shape (Fig. 2). This is the result of minimizing the system's free energy with respect to competing mechanisms. The spherical shape has minimum surface area. But if the anchoring is respected on the drop surface, the interior of the drop will have severe distortions of molecular orientation. The lemon shape emerges as the minimizer for the sum of the interfacial energy, anchoring energy and internal distortional energy. Incidentally, the same argument explains similar lemon shapes if the drop itself is isotropic but the surrounding medium is nematic.[4,5]

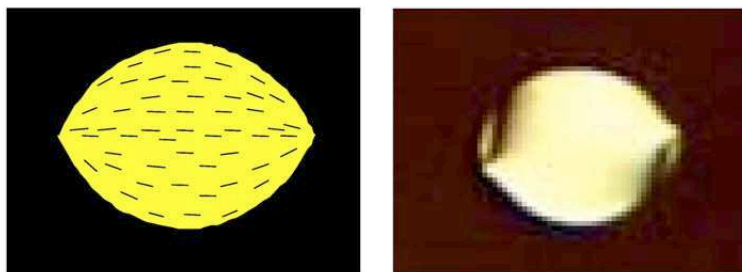342   *Feng, Chen, Yue and Zhou*

Fig. 2.   Non-spherical shape of a liquid crystal drop in an isotropic medium. The image on the right is the micrograph from a polarizing microscope while the one on the left is a sketch of the director orientation field. The length of the drop is about 40 μm. Adapted from Nastishin *et al.*[4] with permission, ©2005 The American Physical Society.

These relatively simple examples highlight the fact that when complex fluids are in contact, their interface often behave anomalously. Ultimately this is because the microstructures in the two bulk phases affect the interfacial behavior. In a broader context, the dynamics of a two-phase complex fluid mixture depends on the coupling among 3 length scales: (i) microstructural configuration, such as the conformation of the polymer chains and the molecular orientation of a liquid crystal; (ii) interfacial morphology; (iii) macroscopic hydrodynamic flow. The coupling between (i) and (iii) is the main subject matter of theoretical rheology.[6] For example, a flow tends to stretch and align the polymer chains. This microstructural change in turn modifies the rheology of the fluid and its resistance to the deformation. Hence the microstructure modifies the flow in return. Similarly, droplet size distribution in an oil-in-water emulsion determines its flow behavior, e.g. viscosity. But shearing of the emulsion as a whole changes the drop size distribution via breakup and coalescence. This features the coupling between (ii) and (iii), which has been studied extensively for Newtonian fluids in two-phase fluid dynamics. This chapter introduces the reader to the fascinating dynamics of multiphase complex fluids that involve all three length scales.

Given the wide range of complex fluids and flow situations, many physical mechanisms may be important.[7] In this chapter, we shall focus on drop dynamics in two types of two-phase complex fluids: one involving a Newtonian fluid and a viscoelastic polymeric liquid, and the other involving a nematic liquid crystal and a Newtonian fluid. For the former, we will analyze an intriguing phenomenon known as partial coalescence, while for the latter, we will investigate the self-assembly of Newtonian droplets sus-
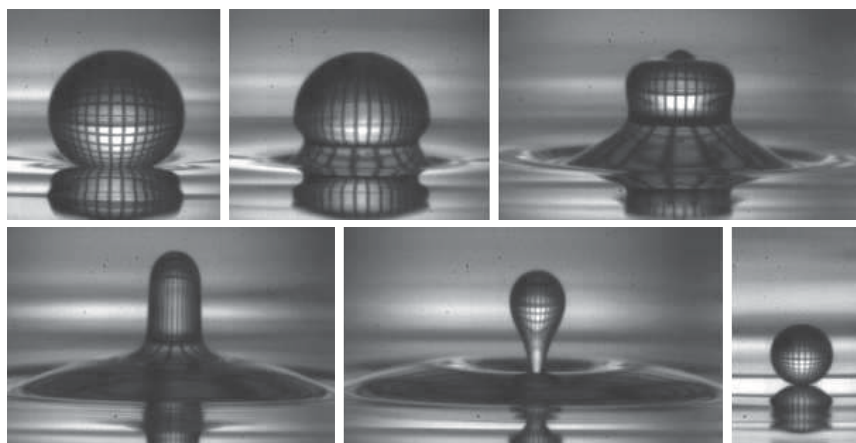
Fig. 3. A cycle in the partial coalescence cascade for an ethanol drop in air. The initial drop diameter is roughly 1.5 mm, and the frames are taken 0, 0.7, 1.8, 3.5, 5 and 50 ms after the initial contact. The grid on the drop comes from background lighting. From Thoroddsen[9] with permission, ©2006 Nature Publishing Group.

pended in a nematic liquid crystal. Obviously, this is not a comprehensive review that covers all known facets of drop dynamics in complex fluids. Rather, our objectives are (i) to give the reader a flavor of the unusual interfacial dynamics that may be encountered in complex fluids, and (ii) to introduce a theoretical model and numerical methods for solving such problems.

2. Partial coalescence in polymer solutions

2.1. *Experimental observations*

Fill a beaker with a liquid, which naturally forms a flat, stationary interface with air. Now gently deposit a drop of the same liquid on the interface. A great deal of surface energy can be saved if the drop coalesces with its homophase below. But to make contact with the liquid below, the drop must first press and squeeze out the cushion of air beneath it. Depending on the drop size and the density of the liquid, the film drainage can take an appreciable length of time.[8] Eventually the air layer gets thin enough that van der Waals forces cause it to rupture, and the drop starts to coalesce with the liquid layer below.

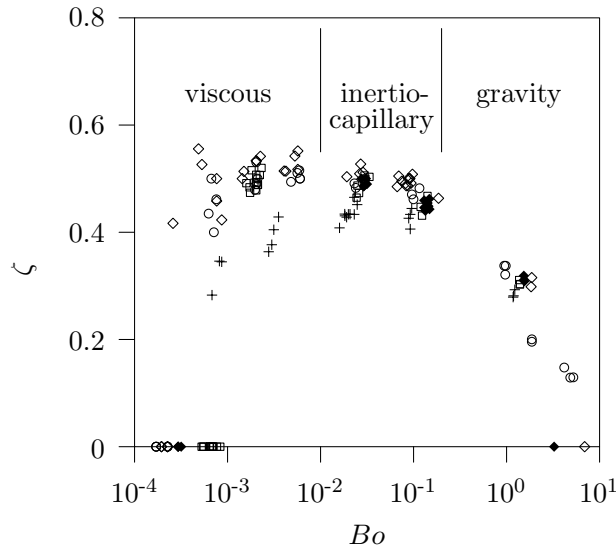Under favorable conditions, the coalescence is not completed at once.

344   *Feng, Chen, Yue and Zhou*

Fig. 4.   The daughter-to-mother drop size ratio ζ as a function of the mother drop size, represented by the Bond number $Bo = \Delta\rho g D^2/\sigma$, $\Delta\rho$ being the density difference, g the gravitational acceleration, D the mother drop diameter, and σ the interfacial tension. $\zeta = 0$ signifies complete coalescence. Different symbols denote different fluid pairs, and for each pair, ζ is taken through the steps of the partial coalescence cascade. Adapted from Chen *et al.*[8] with permission, ©2006 American Institute of Physics.

Instead, a smaller daughter drop is left on the interface (Fig. 3). It then repeats the film drainage process until coalescence, which may leave a still smaller daughter drop on the interface. Such a cascade of *partial coalescence* has been documented with the aid of high-speed video by a number of groups, both for air-liquid systems[10–12] and for liquid-liquid systems.[8,13–17] It has been further discovered that the partial coalescence occurs only for an intermediate range of drop sizes. Drops too large or too small will merge entirely with the underlying liquid in one shot (Fig. 4).

Chen *et al.*[8] explored the same process when the drop (and the underlying liquid) is a viscoelastic polymer solution. The non-Newtonian rheology, as it turns out, tends to suppress partial coalescence; under conditions that would have led to partial coalescence for Newtonian fluids, now the coalescence is completed at once (Fig. 5). Furthermore, if the fluid surrounding the drop is viscoelastic, partial coalescence also tends to be suppressed, although the effect is weaker than if the drop phase is polymeric.

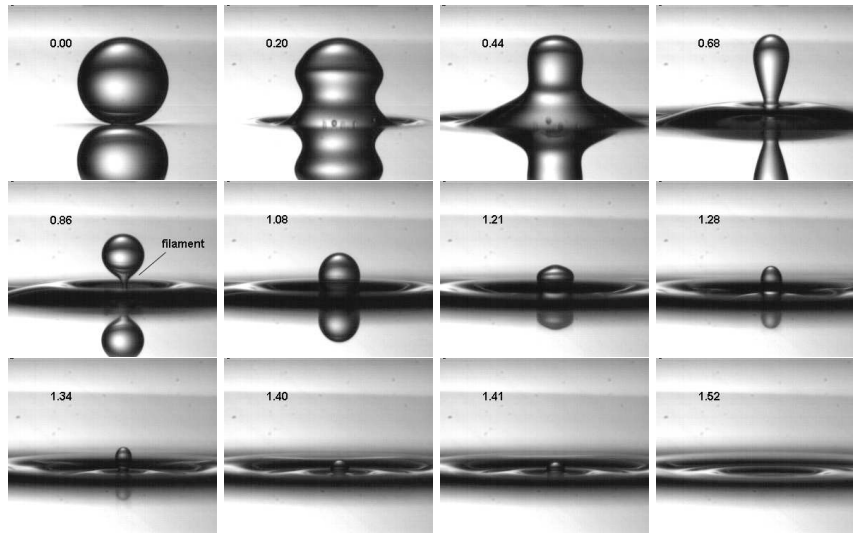This effect can be understood by contrasting the Newtonian and vis-

Fig. 5. Suppression of partial coalescence by viscoelasticity. The drop fluid is a 0.18% solution of poly(ethylene oxide) in water, and the surrounding liquid is decane. The initial drop diameter $D = 1.8$ mm, and the numbers in the frames indicate the advance in time scaled by the capillary time $t_c = (\rho D^3/\sigma)^{1/2}$. From Chen *et al.*[8] with permission, ©2006 American Institute of Physics.

coelastic scenarios depicted in Figs. 3 and 5. The initial rupture of the cushioning fluid sends a capillary wave up the drop. Simultaneously, a capillary wave also ripples out on the interface but this is not directly related to our argument. In time, the drop turns into an elongated column; see the fourth frame of Fig. 3 and the third frame of Fig. 5. This process is driven by surface energy being turned first into kinetic energy in the wave motion, and then into gravitational potential energy of the column. Up to this point, the Newtonian and viscoelastic behaviors are qualitatively the same. But a viscous liquid column longer than its circumference is subject to the Rayleigh instability as mentioned in the Introduction. Thus, the column in Fig. 3 forms a neck that pinches off in time, producing the daughter drop and partial coalescence. For the viscoelastic column of Fig. 5, on the other hand, the same stabilizing effect as evident in the beads-on-a-string formation of Fig. 1 comes into play. A neck forms and turns into a thin filament, as indicated in Frame 5 of Fig. 5, which persists without breaking up. In time the drop fluid drains down the filament and the shrinking drop falls and merges into the underlying polymer solution. To explain the in-

Feng, Chen, Yue and Zhou

verted case of a Newtonian drop in a polymeric upper liquid, Chen *et al.*[8] observed the breakup of a Newtonian filament in a polymer solution, and found that it is subject to the same type of stabilization with the formation of beads on the thinning thread.

To understand why partial coalescence appears only for an intermediate range of drop sizes, one needs to examine the time scales of two competing mechanisms. If it takes longer to drain the drop through the neck than for the neck to pinch off, the latter occurs and leaves a daughter drop behind. Conversely, if the drop drains into the lower layer before the neck pinches off, complete coalescence results. For drops that are too large, gravity dominates and the drop practically collapses into the bottom layer in one shot. For drops that are too small, viscosity dominates and slows down the thinning of the neck so complete merging takes place. In the intermediate range, a balance between capillarity and inertia produces a self-similar regime in which the drop diameter shrinks approximately by one half through each cycle of the cascade.[10,16] Chen *et al.*[8] have documented how viscoelasticity in either component narrows down the range of drop sizes for partial coalescence.

To reflect on an argument advanced in the Introduction, the suppression of partial coalescence by viscoelasticity provides an example that clearly demonstrates how bulk rheology qualitatively modifies the behavior of the interface. In this case, the rheology is manifested by "strain hardening", namely a steep increase in elongational viscosity during straining. Its molecular origin is the stretching and alignment of polymer chains by the elongational flow. While the explanation given above sounds reasonable, it needs to be confirmed by a quantitative study of the fluid mechanical process. This will be accomplished by numerical computations in the following.

2.2. *Numerical simulations*

Laminar flows of incompressible Newtonian fluids are governed by the Navier-Stokes equations:

$$\nabla \cdot \boldsymbol{v} = 0, \tag{1}$$

$$\rho \left(\frac{\partial \boldsymbol{v}}{\partial t} + \boldsymbol{v} \cdot \nabla \boldsymbol{v} \right) = -\nabla p + \nabla \cdot \boldsymbol{\tau}, \tag{2}$$

$$\boldsymbol{\tau} = \mu[\nabla \boldsymbol{v} + (\nabla \boldsymbol{v})^{\mathrm{T}}], \tag{3}$$

where $\boldsymbol{v}$ and p are the velocity and pressure in the fluid, ρ and μ are the density and viscosity. The stress tensor $\boldsymbol{\tau}$ is related to the velocity gradi-

ent linearly for a Newtonian viscous fluid. Computational fluid dynamics is concerned mostly with solving this set of partial differential equations subject to proper boundary conditions.

If the fluid is non-Newtonian, $\boldsymbol{\tau}$ depends on the fluid deformation in a more complex way. For viscoelastic liquids, in particular, $\boldsymbol{\tau}$ depends not only on the deformation at the current moment, but also the history of deformation. Hence comes the idea of "memory" and elasticity. For a systematic exposition on rheology and constitutive modeling, the reader may consult several monographs.[1,6,7,18] For our purpose, it suffices to give the Giesekus equation as an example of viscoelastic constitutive equations:

$$\boldsymbol{\tau} = \boldsymbol{\tau}_p + \boldsymbol{\tau}_s, \tag{4}$$

$$\boldsymbol{\tau}_s = \mu_s[\nabla \boldsymbol{v} + (\nabla \boldsymbol{v})^{\mathrm{T}}], \tag{5}$$

$$\boldsymbol{\tau}_p + \lambda_H \boldsymbol{\tau}_{p(1)} + \alpha \frac{\lambda_H}{\mu_p} \boldsymbol{\tau}_p \cdot \boldsymbol{\tau}_p = \mu_p[\nabla \boldsymbol{v} + (\nabla \boldsymbol{v})^{\mathrm{T}}], \tag{6}$$

where the total stress tensor $\boldsymbol{\tau}$ is the sum of a Newtonian solvent contribution $\boldsymbol{\tau}_s$ and a polymer stress $\boldsymbol{\tau}_p$. In the partial differential equation governing $\boldsymbol{\tau}_p$, the subscript (1) denotes the so-called upper-convected derivative:

$$\boldsymbol{\tau}_{p(1)} = \frac{\partial \boldsymbol{\tau}_p}{\partial t} + \boldsymbol{v} \cdot \nabla \boldsymbol{\tau}_p - (\nabla \boldsymbol{v})^{\mathrm{T}} \cdot \boldsymbol{\tau}_p - \boldsymbol{\tau}_p \cdot \nabla \boldsymbol{v}. \tag{7}$$

λ_H and α are respectively the relaxation time and mobility parameter of the model, and μ_s and μ_p are the solvent and polymer viscosities. The numerical solution of non-Newtonian flows is a great deal more complex than that of Newtonian flows, and interested readers are referred to Owens and Phillips.[19]

If one deals with flow of two immiscible components, the situation is also more complex because now the fluid domain contains internal boundaries that deform and move. The motion of the interfaces is most conveniently described in Lagrangian terms, while the Navier-Stokes equations are customarily solved in an Eulerian framework. The crux is in reconciling these two viewpoints. A conceptually straightforward treatment is to lay grid points on the internal boundaries, which will track the interfacial motion in every time step. The governing equations are solved for each component, with matching boundary conditions on the interface. This typically calls for a moving grid and periodic remeshing and interpolation.[20] Besides the computational overhead, a limitation of these *interface-tracking* methods is the appearance of singularities when interfaces merge and rupture. An alternative is the *interface-capturing* methods, which introduce an auxiliary scalar field to demarcate the two components and indicate the location

348 *Feng, Chen, Yue and Zhou*

of the interface.[21] The scalar field evolves according to a postulated convection or convection-diffusion equation. Thus, the computational burden of tracking the interface is replaced by that of solving an additional evolution equation. The main attractions are (i) now the governing equations can be solved over the entire domain on an Eulerian grid, with no need to match the boundary conditions on the interface; (ii) topological changes of the interface, such as rupture, can be handled more naturally. The most widely used interface-tracking methods include the volume-of-fluid method, the level-set method and the diffuse-interface method.

The computations to be described here are based on the diffuse-interface method.[22] We imagine the two components, although nominally immiscible, nevertheless mix to a slight degree over a narrow interfacial region. We define a phase-field variable ϕ as a scaled "concentration" such that $\phi = -1$ in fluid bulk A and $\phi = +1$ in B, and the interface is traced out by the level curve of $\phi = 0$. We further require the evolution of ϕ be governed by the Cahn-Hilliard equation:[23,24]

$$\frac{\partial \phi}{\partial t} + \boldsymbol{v} \cdot \nabla \phi = \gamma \lambda \nabla^2 \left[-\nabla^2 \phi + \frac{\phi(\phi^2 - 1)}{\epsilon^2} \right], \qquad (8)$$

where γ is the Cahn-Hilliard mobility parameter, λ is the density of the mixing energy between the two components, and ϵ is the capillary width. This is a phenomenological model based on the ideas that the evolution of ϕ is governed by a mixing energy in the diffuse interface, and that the species diffuse across the interfaces as driven by gradients of the chemical potential.[25] The equilibrium ϕ profile is a minimizer of the mixing energy, and has the characteristic sigmoidal shape sketched in Fig. 6. The interfacial tension can be shown to be related to the Cahn-Hilliard model parameters as

$$\sigma = \frac{2\sqrt{2}}{3} \frac{\lambda}{\epsilon}, \qquad (9)$$

and the interfacial thickness, say defined between $\phi = \pm 0.9$, is roughly 5ϵ. Feng *et al.*[22] have given a general review of the theoretical background of the model, as well as its computational implementation for simulating two-phase flows. We only mention that for the problems at hand, this formalism enjoys the advantage that the moving interface and viscoelastic rheology can be handled in a unified framework based on the free energy.

The numerical solution of the continuity and momentum equations (1, 2), the constitutive equations (4–6) and the Cahn-Hilliard equation (8) is a daunting task. Beside the complexity of the equations, the numerical
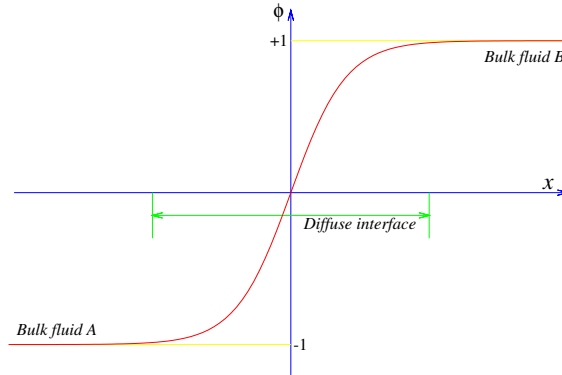
Drop Dynamics in Complex Fluids   349

Fig. 6.   Sketch of the phase-field profile across the diffuse interface.

challenge lies in resolving the thin interfacial profile adequately so the in-
terfacial tension can be computed accurately. Over the past few years, we
have developed a finite-element package AMPHI that uses finite-elements
with a novel adaptive meshing scheme. The scope of this chapter does not
allow a detailed discussion of the algorithm, for which we refer the reader
to Yue *et al.*[26,27] In the following, we focus on using this methodology to
simulate the partial coalescence phenomenon in Newtonian and viscoelas-
tic liquids. Axisymmetry is always assumed in the geometric setup of the
simulation.

   As a validation of the diffuse-interface model and the numerical algo-
rithm, we first tried to reproduce the partial coalescence experiment for
Newtonian liquids, with a water drop above a decane-water interface.[28]
The calculation uses the true densities and viscosities of water and decane,
and proper values for λ and ϵ to produce the correct interface tension σ.
Figure 7 gives a frame-by-frame comparison between experiment and simu-
lation for one cycle of partial coalescence. The experimental snapshots are
separated by a fixed interval of 542 μs, and the time below each gives the
time for the numerical picture that best matches the experimental snapshot.
Therefore, following the initial rupture at $t = 0$, the numerical simulation
accurately reproduces the progress of the coalescence, from the propagation
of the capillary wave up the drop (a–e) to the formation of a liquid column
(e–g), and finally to the formation of a neck (g–i). The next 2 frames,
however, covers the pinchoff of the neck that generates the daughter drop.
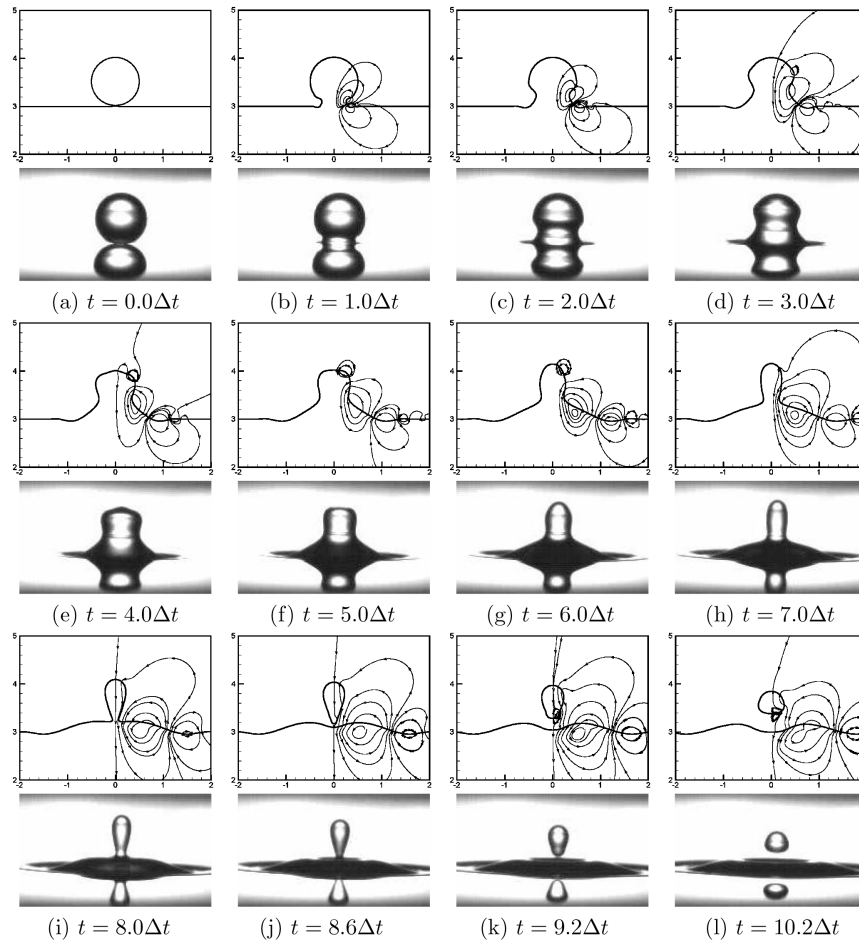
Feng, Chen, Yue and Zhou

Fig. 7.   Frame-by-frame comparison between observation and computation of one cycle of partial coalescence. Streamlines in the computational plot indicate the local flow field. From Yue *et al.*[28] with permission, ©2006 American Institute of Physics.

This is when the numerical simulation fails to track the progression in the correct time. Instead, the pinchoff occurs some 40% faster numerically than in reality. After the daughter drop is formed (k), the simulation again captures the real event precisely.

The discrepancy for frames (j) and (k) highlights a fundamental limitation to the diffuse-interface method. In reality, interfaces between small-molecule liquids are nanometers thick. If the drop itself is millimeters in
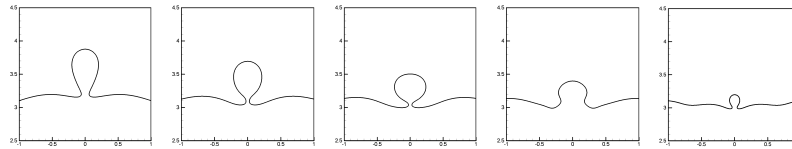
Fig. 8.   Suppression of partial coalescence by viscoelasticity. The drop and lower fluid is a viscoelastic Giesekus fluid, while the upper layer is a Newtonian fluid. From left to right, the snapshots are at dimensionless times $t = 0.740$, 0.837, 0.934, 1.04 and 1.19, scaled by the capillary time t_c. From Yue *et al.*[28] with permission, ©2006 American Institute of Physics.

diameter, there is a gap of 10^6 in length scales that needs to be bridged. For the current generation of computational power and algorithms, it is impossible to fully resolve the minute details within the interfacial profile, as a diffuse-interface method must, while covering the drop-scale hydrodynamics at the same time. Thus, the interfacial thickness in the simulations, given by ϵ, is typically much larger than the real values. Experience shows that once the ratio $Cn = \epsilon/D$, known as the Cahn number, falls below a threshold on the order of 10^{-2}, the numerical result becomes independent of Cn in most situations.[25,26] This is when the *sharp interface limit* is reached, a necessary condition for the model predictions to be physically meaningful. The pinchoff in Fig. 7 is an exception to this rule in that the physical length scale of interest, say the neck radius, tends to zero. Thus, the $Cn = 5 \times 10^{-3}$ used, sufficiently small up to frame (i), eventually becomes too large as the neck pinches off. Two thicker interfaces start to overlap and interact sooner than thinner ones, and so the numerical simulation proceeds faster than reality. Thus, the diffuse-interface model can be a powerful and in some sense unique tool for computing interfacial flows, but one has to be aware of its inherent limitations. That partial coalescence occurs only for a range of drop sizes, being suppressed by gravity and viscosity on either end of the range, has also been reproduced numerically.[28]

Turning now to the role of viscoelasticity in suppressing partial coalescence, we use the Giesekus constitutive equation (6), with model parameters fitted roughly to the rheology of the polymer solutions. Figure 8 shows the evolution of the interfaces for a polymer drop surrounded by a Newtonian oil. The neck forms but the thin thread persists without breaking, as seen experimentally in Fig. 5. Note the close proximity of the dimensionless times between the experiment and the simulation. To confirm the explanation proposed before, we plot the flow and polymer stress fields when the
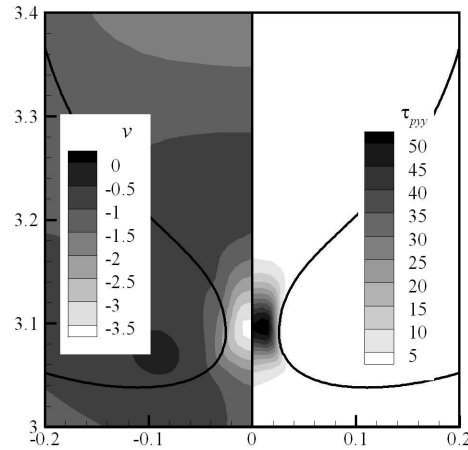
Feng, Chen, Yue and Zhou

Fig. 9.   Flow and stress fields near the neck for the viscoelastic drop in the second frame of Fig. 8, $t = 0.837$. The left half shows contours of the vertical velocity scaled by D/t_c. The right half shows contours of the polymer stress component τ_{pyy} scaled by σ/D. From Yue *et al.*[28] with permission, ©2006 American Institute of Physics.

neck is at its thinnest (Fig. 9). It is evident that the strong polymer tensile stress, due to the strain-hardening rheology, resists continued stretching and thinning of the neck, and suppresses partial coalescence. A similar scenario occurs when the viscoelasticity occurs in the surrounding fluid.[28] There the polymer stress is activated indirectly through the no-slip boundary condition on the interface; pinchoff of the neck requires stretching of the surrounding fluid as well, which is resisted by the polymer stress.

3. Droplet self-assembly in nematic liquid crystals

3.1. *Experimental observations*

More than a decade ago, Poulin and coworkers[29] reported that water droplets suspended in a nematic liquid crystal (LC) organize themselves into a chain, with a more or less constant spacing between neighboring droplets. This was later confirmed by spectacular pictures of parallel chains that form by self-assembly of silicone oil droplets in a nematic medium[30] (Fig. 10a). More recently, 2D colloidal crystals have been made via self-assembly of colloidal particles in a nematic LC[31] (Fig. 10b).

(a)   (b)
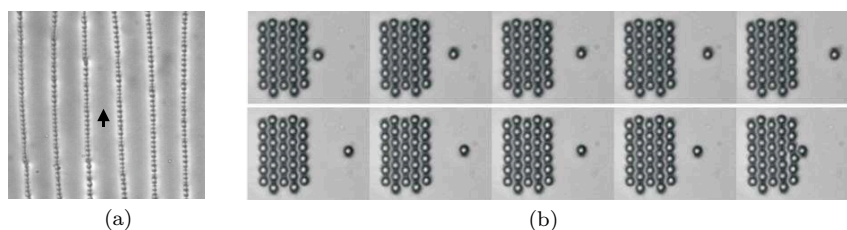
Fig. 10.   (a) Silicone oil droplets, about 2 μm in size, arrange themselves into roughly equally spaced lines along the direction of the nematic director (indicated by the black arrow). Adapted from Loudet *et al.*[30] with permission, ©2000 Macmillan Magazines Ltd. (b) Chains of silica particles, 2.32 μm in diameter, are coaxed into forming a regular 2D crystal in a nematic LC. From left to right, the frames at advancing times show the interaction between the single particle and the chains, which is discussed later in the text. Adapted from Musevic *et al.*[31] with permission, ©2006 by the American Association for the Advancement of Science.

The key to such pattern formation is topological defects created by droplets or particles inserted into an otherwise uniformly oriented LC. Nematic LC consists of anisotropic — rodlike or disclike — molecules that are more or less aligned with each other.[32] This produces a local average orientation that is conventionally marked by a unit vector $\boldsymbol{n}$ called the director. There is also long-range order in nematic LC in that any spatial distortion of the $\boldsymbol{n}$ field, in terms of the gradient $\nabla\boldsymbol{n}$, is resisted by distortional elasticity. Besides this bulk elasticity, LC molecules also have a preferred anchoring direction on surfaces, the most common ones being homeotropic (perpendicular) and planar (tangential) anchoring. Thus, when a water droplet with homeotropic anchoring is inserted into an LC single crystal, the radial $\boldsymbol{n}$ field near the droplet comes into conflict with the uniform far field. This conflict is resolved by nucleating a topological defect. For homeotropic anchoring, two potential configurations are depicted in Fig. 11 with either a point defect or a line defect. These are aptly called the satellite point defect and the Saturn ring defect, respectively. Both numerical computations and direct observations have confirmed their existence, and their stability relative to each other has been investigated extensively.[33–37] For planar anchoring, surface defects called boojums prevail,[34] but these are not relevant to the self-assembly of interest here.

Poulin and coworkers[29,30] observed that water and silicone-oil droplets exhibit homeotropic anchoring on the interface, and that when droplets line up into regular chains, each is always accompanied by a satellite point defect. They proposed an explanation for the self-assembly based on an

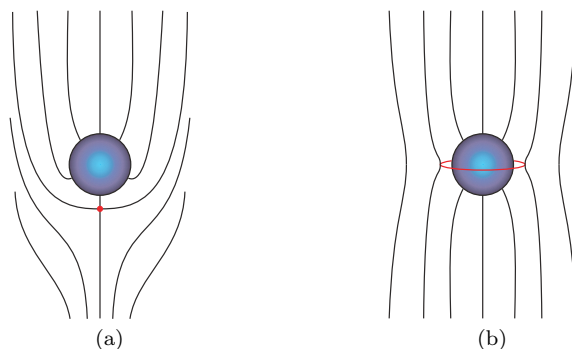354   *Feng, Chen, Yue and Zhou*

Fig. 11.   Sketch of the satellite point defect (a) and Saturn ring defect (b) near a droplet with homeotropic anchoring. The solid lines trace out the director orientation.

analogy to electric dipoles. The droplet and its satellite point defect form a dipole, say pointing from the drop center to the defect. When two droplets are nearby, they interact through the equivalent of dipole-dipole attraction in electrostatics. Of course, the physical origin of the attraction is different here: when two droplets have their satellite defects on their line of centers and on the same side, elastic distortional energy is reduced when the two move toward each other until an optimal center-to-center separation of roughly 2.6a, a being the drop radius.[29] Thus, droplets form a line with uniform spacing between neighbors along the direction of the background nematic director.

The same analogy also explains the repulsion between two chains in parallel, with their dipoles pointing in the same direction. Thus, the parallel chains maintain a more or less equal distance from each other in Fig. 10a. Furthermore, two chains with their dipolar directions opposite to each other (anti-parallel) should attract each other, and this explains the formation of the regular 2D arrays in Fig. 10b consisting of chains of alternating dipole directions. The top row of images in Fig. 10b shows a single droplet, with a dipole parallel to the nearby chain, being pushed away. In the bottom row, a single particle with a dipole anti-parallel to the nearby chain is attracted toward it.

But the drop-defect pair can be seen as a dipole only when viewed from a large distance, i.e., when neighboring drops are far apart. When their separation is on the order of the drop diameter, the interaction is necessarily more complex. To gain a more direct understanding of the physics underlying the self-assembly, we have carried out numerical computations to

probe both the pairwise interaction between two droplets and the dynamic process of self-assembly.

3.2. *Numerical simulations*

The simulations are based on the same diffuse-interface model explained above. However, the microstructure of the nematic LC, namely the molecular orientation represented by the director $\boldsymbol{n}$, leads to a more complex mathematical model. The LC itself possesses a solid-liquid duality; it flows like a liquid but resists orientational distortion and transmits torque like an elastic solid. The former is characterized by 6 anisotropic Leslie viscosities and the latter by a linear Frank elasticity theory. The two are integrated in the Ericksen-Leslie theory for LC hydrodynamics,[32] which will be used in our computations. Since we have a diffuse interface between the isotropic and nematic liquids, the anchoring condition requires a careful treatment. Besides, the defect normally presents a singularity in the $\boldsymbol{n}$ field, and is regularized here using a variable order parameter near the defect core. Details of the derivation can be found in the literature.[5,25,38,39] For a mixture of a nematic (marked by $\phi = 1$) and a Newtonian viscous liquid ($\phi = -1$), the governing equations are:

$$\nabla \cdot \boldsymbol{v} = 0, \tag{10}$$

$$\rho \left(\frac{\partial \boldsymbol{v}}{\partial t} + \boldsymbol{v} \cdot \nabla \boldsymbol{v} \right) = -\nabla p + \nabla \cdot \boldsymbol{\sigma}, \tag{11}$$

$$\frac{\partial \phi}{\partial t} + \boldsymbol{v} \cdot \nabla \phi = \gamma \lambda \nabla^2 \left[-\nabla^2 \phi + \frac{\phi(\phi^2 - 1)}{\epsilon^2} \right], \tag{12}$$

$$\boldsymbol{h} = \gamma_1 \boldsymbol{N} + \gamma_2 \boldsymbol{D} \cdot \boldsymbol{n}. \tag{13}$$

Equation (13) governs the evolution of the $\boldsymbol{n}$ field subject to elastic and viscous torques. The molecular field vector $\boldsymbol{h}$ represents the elastic torque:

$$\boldsymbol{h} = K \left[\nabla \cdot \left(\frac{1+\phi}{2} \nabla \boldsymbol{n} \right) - \frac{1+\phi}{2} \frac{(\boldsymbol{n} \cdot \boldsymbol{n} - 1)\boldsymbol{n}}{\delta^2} \right] - \boldsymbol{g}, \tag{14}$$

where K is the bulk elastic constant, δ is a small defect core size used for regularizing the defect, and $\boldsymbol{g} = A[(\nabla\phi \cdot \nabla\phi)\boldsymbol{n} - (\boldsymbol{n} \cdot \nabla\phi)\nabla\phi]$ for homeotropic anchoring, A being the anchoring energy. The time derivative of $\boldsymbol{n}$ is embedded in the vector $\boldsymbol{N} = \frac{d\boldsymbol{n}}{dt} - \frac{1}{2}[(\nabla\boldsymbol{v})^{\mathrm{T}} - \nabla\boldsymbol{v}] \cdot \boldsymbol{n}$, which is the rotation of $\boldsymbol{n}$ with respect to the background flow field. $\boldsymbol{D} = \frac{1}{2}[\nabla\boldsymbol{v} + (\nabla\boldsymbol{v})^{\mathrm{T}}]$ is the strain rate tensor, and γ_1 and γ_2 are viscosity coefficients. The stress

tensor

$$\boldsymbol{\sigma} = -\lambda \nabla \phi \nabla \phi - K \frac{1+\phi}{2}(\nabla \boldsymbol{n}) \cdot (\nabla \boldsymbol{n})^{\mathrm{T}} - \boldsymbol{G} + \frac{1+\phi}{2}\boldsymbol{\sigma'} + (1-\phi)\mu \boldsymbol{D},\ (15)$$

with $\boldsymbol{G} = A[(\boldsymbol{n}\cdot\boldsymbol{n})\nabla\phi - (\boldsymbol{n}\cdot\nabla\phi)\boldsymbol{n}]\nabla\phi$ for homeotropic anchoring, and μ being the viscosity of the Newtonian component. $\boldsymbol{\sigma'}$ is the Leslie viscous stress in the nematic phase[40]

$$\boldsymbol{\sigma'} = \alpha_1 \boldsymbol{D} : \boldsymbol{nnnn} + \alpha_2 \boldsymbol{nN} + \alpha_3 \boldsymbol{Nn} + \alpha_4 \boldsymbol{D} + \alpha_5 \boldsymbol{nn}\cdot \boldsymbol{D} + \alpha_6 \boldsymbol{D}\cdot \boldsymbol{nn},\ (16)$$

where α_1 to α_6 are the Leslie viscous coefficients observing the Onsager relationship:[32] $\alpha_2 + \alpha_3 = \alpha_6 - \alpha_5$. The coefficients $\gamma_1 = \alpha_3 - \alpha_2$ and $\gamma_2 = \alpha_3 + \alpha_2$.

The numerical algorithm is essentially the same as used in Sec. 2.2, except that now the point defect, as well as the interface, requires locally refined grid for accurate resolution of the sharp gradients $\boldsymbol{n}$. For details see Yue *et al.*[26] and Zhou *et al.*[39] In all the simulations to be discussed, we use a relatively large interfacial tension so that the drops remain essentially spherical in all times. This is true in the experimental observations, and also simplifies the analysis of the results by excluding the effect of drop deformation, which was essentially absent in the experimental systems. For an example of LC anchoring coupling with drop deformation, see Zhou *et al.*[5]

First, we place two droplets in the so-called parallel configuration, with their "dipoles" in the same direction and along their line of centers. The computational domain is axisymmetric in this case. Under the effect of distortional elasticity, the droplets start to move toward each other (Fig. 12a). From this motion, one can estimate the elastic driving force on each droplet from the Stokes drag by neglecting inertia and assuming that the drop is in force balance during the approach. This estimate turns out to be slightly below the true force computed from integrating the stress over the interface. Both forces are compared with prior theoretical and experimental results in Fig. 12b. The long-range attraction manifests a R^{-4} scaling, as is expected from the attraction between two electric dipoles given by Lubensky *et al.*[34] As the separation decreases, however, the attraction force decreases sharply, falling below the dipole formula, and approaches zero toward $R = 2.45a$. If the two droplets were initially placed closer than the equilibrium separation, they separate until $R = 2.45a$. The two experimental data sets indicate that the $F \propto R^{-4}$ power-law persists to smaller separations. But the equilibrium separation corresponding to $F = 0$ is in close agreement between computation and observations.
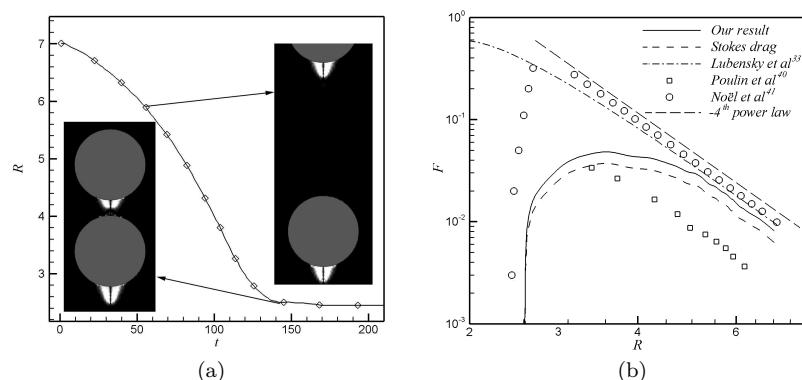
Fig. 12.   Attraction between two droplets bearing satellite point defects placed in the parallel configuration. (a) The distance between the centers of the droplets decreasing as the two droplets attract each other. The two insets show the birefringence patterns around the defects computed from the director field. The point defect sits at the tip of the two bright lobes. (b) The attraction force as a function of the droplets' separation, compared with the dipole formula[34] and experimental data.[41,42] Note that both axes are in logarithmic scale and the long-range attraction exhibits a $F \sim R^{-4}$ power law. Adapted from Zhou *et al.*[39] with permission, ©2008 by the American Chemical Society.

The dynamic simulation of droplet interaction thus confirms the idea that the long-range attraction between droplets in the parallel configuration resembles dipolar attraction. For smaller separations, the idea of dipole-dipole attraction no longer applies, and it certainly cannot account for the equilibrium separation and the repulsion between droplets that are too close to each other. This is where the dynamic computation provides results and insight that cannot come from the heuristic argument. Going beyond pairwise attraction, Zhou *et al.*[39] have confirmed that a group of droplets in a 2D domain indeed form a chain along the undisturbed nematic director.

To probe sidewise interactions between chains of droplets, we arrange two chains in initial configurations with their "dipoles" either in the same direction (parallel) or reversed (anti-parallel). These computations are done in a 2D planar domain. Figure 13 demonstrates that the parallel chains repel each other, while the anti-parallel chains attract each other. These trends are in qualitative agreement with the experimental observations in Fig. 10b. The anti-parallel chains eventually approach an equilibrium separation of $2.44a$, which is close to the observed value of $2.31a$ by Musevic *et al.*[31] despite the two-dimensionality of the computations.

The interaction can be understood from the director patterns. For the
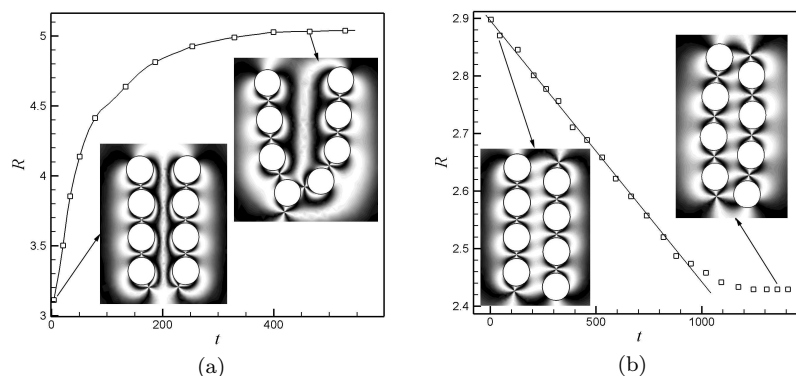
Feng, Chen, Yue and Zhou

Fig. 13.   Lateral interaction between chains of droplets. (a) The chains in the parallel configuration, with their dipoles in the same direction, repel each other. (b) The chains in the anti-parallel configuration, with their dipoles in the opposite direction, attract each other. The grayscale contours are for $(n_x^2 - 1/2)^2$, n_x being the horizontal component of the director, such that white indicates a vertical or horizontal $\boldsymbol{n}$ and black means a $45°$ tilt. Adapted from Zhou *et al.*[39] with permission, ©2008 by the American Chemical Society.

parallel configuration sketched in Fig. 14a, the director $\boldsymbol{n}$ is forced to make a sharp upward turn between the chains. This is reflected in Fig. 13a by the narrow vertical dark and bright bands between the chains. The closer the two chains, the more severe the spatial distortion in between and the greater the elastic energy. Thus, the two chains repel each other. Note, however, the unexpected break of symmetry in the dynamic simulation of Fig. 13a. The bottom droplet on the right chain has rotated its dipole clockwise so as to point its satellite defect toward the bottom droplet of the left chain. This created an attraction similar to Fig. 12 and pulls the two bottom droplets toward each other. In the anti-parallel configuration of Fig. 14b, the director field merges smoothly between the two chains, with $\boldsymbol{n}$ assuming a relatively uniform, horizontal orientation. This $\boldsymbol{n}$ field has lower distortional energy than if the chains are far apart, which explains the attraction between the chains. If they are too close together, however, the radial $\boldsymbol{n}$ field surrounding each droplet comes into direct conflict, resulting in greater distortion and higher energy. The minimum-energy state is the equilibrium with a separation of $2.44a$ between the chains.

Finally, we place 8 identical droplets in random positions in a doubly periodic 2D domain, and observe their self-assembly (Fig. 15). The drop-drop interaction is dominated by longitudinal dipole-like attractions (when
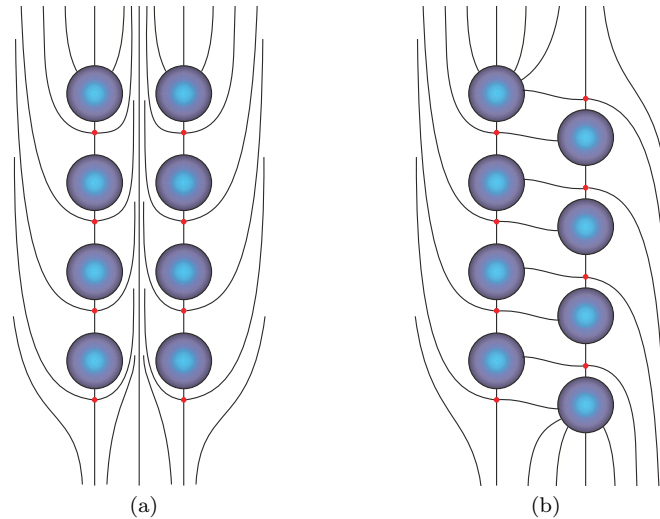
Fig. 14. Sketch of the director field around two chains of droplets. (a) The parallel configuration with the same dipolar orientation for the chains. (b) The anti-parallel configuration with opposite dipolar orientations.

nearby droplets have their satellite defects on their line of centers) and sideways repulsions (when their dipoles are in the parallel configuration). For example, drops 3, 5 and 7 initially move away from each other sideways. Then drop 5 is attracted by drop 6, and is eventually pulled in between drops 3 and 6 to form a diagonal chain. Drops 1, 4 and 2 seem to form a vertical chain by themselves. Since the domain is doubly periodic, there is no prescribed background nematic orientation to which a chain may align. Thus, the two chains spontaneously assume different angles. Conceivably, they will eventually line up into a single long chain, although our domain would not be large enough to accommodate that. Despite the small number of droplets in the simulation, the dynamic scenario of self-assembly exhibits the main features observed in reality (cf. Fig. 10a), and confirms that pairwise attraction (longitudinal) and repulsion (lateral) are the dominant mechanisms at play.

4. Summary

To recapitulate, we have described two intriguing phenomena in drop dynamics involving polymer solutions and nematic liquid crystals, and demon-
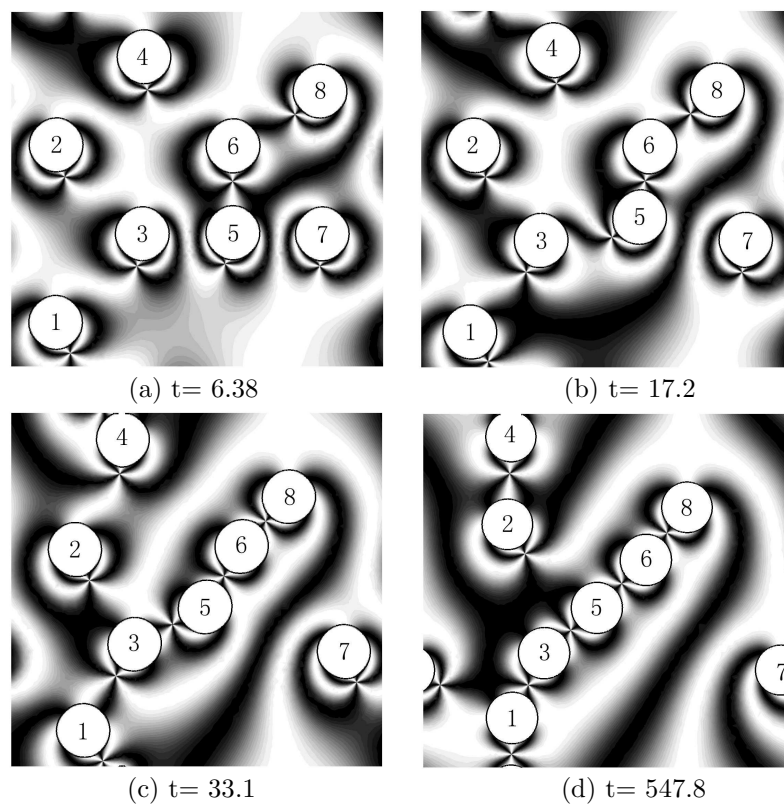
360   *Feng, Chen, Yue and Zhou*

(a) t= 6.38

(b) t= 17.2

(c) t= 33.1

(d) t= 547.8

Fig. 15.   Self-assembly of 8 drops in a doubly periodic domain. Time is made dimensionless by $\eta a^2/K$. Adapted from Zhou *et al.*[39] with permission, ©2008 by the American Chemical Society.

strated how numerical computation based on a diffuse-interface model can provide explanations to the experimental observations. The main insights from this chapter are:

(1) The interface between complex fluids may exhibit behavior qualitatively different from that for Newtonian fluids.
(2) The cause of such behavior should be sought from the coupling among microstructural conformation, interfacial morphology and large-scale fluid flow.
(3) Numerical computation is a powerful tool that can be used to gain

an understanding of the physical mechanisms that would otherwise be difficult to obtain.

The above insights, although derived from two specific examples, is relevant to all two-component complex fluids having internal boundaries. In the case of drop-interface partial coalescence, it is the strain-hardening rheology of the polymeric component, a direct manifestation of molecular alignment and stretching, that suppresses partial coalescence under suitable conditions. In the case of droplets self-assembling in a nematic suspending medium, it is the distortional elasticity in the bulk and anchoring on the interfaces, both originating from the molecular orientation, that drive the maneuver of the droplets relative to each other.

As mentioned at the beginning, the purpose of the chapter is not to provide a comprehensive summary of the literature on drop dynamics in complex fluids. Instead, we use concrete examples to illustrate the rich dynamics of interfaces between complex fluids, and demonstrate a theoretical model and numerical technique that are well suited for this type of problems. We hope that the chapter has aroused the readers' interest in such problems, and given them the basic ideas for formulating a research approach to similar systems in their own work.

Acknowledgments

References

1. R. B. Bird, R. C. Armstrong, and O. Hassager, *Dynamics of Polymeric Liquids, Vol. 1. Fluid Mechanics.* (Wiley, New York, 1987).
2. P. G. Drazin and W. H. Reid, *Hydrodynamic Stability.* (Cambridge University Press, New York, 1981).
3. M. S. N. Oliveira and G. H. McKinley, Iterated stretching and multiple beads-on-a-string phenomena in dilute solutions of highly extensible flexible polymers, *Phys. Fluids.* **17**, 071704, (2005).
4. Y. A. Nastishin, H. Liu, T. Schneider, V. Nazarenko, R. Vasyuta, S. V. Shiyanovskii, and O. D. Lavrentovich, Optical characterization of the ne-

Feng, Chen, Yue and Zhou

matic lyotropic chromonic liquid crystals: Light absorption, birefringence, and scalar order parameter, *Phys. Rev. E.* **72**, 041711, (2005).

5. C. Zhou, P. Yue, J. J. Feng, C. Liu, and J. Shen, Heart-shaped bubbles rising in anisotropic liquids, *Phys. Fluids.* **19**, 041703, (2007).

6. R. B. Bird, C. F. Curtiss, R. C. Armstrong, and O. Hassager, *Dynamics of Polymeric Liquids, Vol. 2. Kinetic Theory.* (Wiley, New York, 1987).

7. R. G. Larson, *The Structure and Rheology of Complex Fluids.* (Oxford, New York, 1999).

8. X. Chen, S. Mandre, and J. J. Feng, An experimental study of the coalescence between a drop and an interface in newtonian and polymeric liquids, *Phys. Fluids.* **18**, 092103, (2006).

9. S. T. Thoroddsen, Droplet genealogy, *Nature Phys.* **2**, 223–224, (2006).

10. S. T. Thoroddsen and K. Takehara, The coalescence cascade of a drop, *Phys. Fluids.* **12**(6), 1265–1267, (2000).

11. E. M. Honey and H. P. Kavehpour, Astonishing life of a coalescing drop on a free surface, *Phys. Rev. E.* **73**, 027301, (2006).

12. F. Blanchette and T. P. Bigioni, Partial coalescence of drops at liquid interfaces, *Nature Phys.* **2**, 254–257, (2006).

13. G. E. Charles and S. G. Mason, The mechanism of partial coalescence of liquid drops at liquid/liquid interfaces, *J. Colloid Sci.* **15**, 105–122, (1960).

14. Z. Mohamed-Kassim and E. K. Longmire, Drop coalescence through a liquid/liquid interface, *Phys. Fluids.* **16**, 2170–2181, (2004).

15. A. D. Nikolov and D. T. Wasan, Effects of surfactant on multiple stepwise coalescence of single drops at liquid-liquid interfaces, *Ind. Eng. Chem. Res.* **34**, 3653–3661, (1995).

16. X. Chen, S. Mandre, and J. Feng, Partial coalescence between a drop and a liquid-liquid interface, *Phys. Fluids.* **18**, 051705, (2006).

17. T. Gilet, K. Mulleners, J. P. Lecomte, N. Vandewalle, and S. Dorbolo, Critical parameters for the partial coalescence of a droplet, *Phys. Rev. E.* **75**, 036303, (2007).

18. R. I. Tanner, *Engineering Rheology.* (Oxford, New York, 2000).

19. R. G. Owens and T. N. Phillips, *Computational Rheology.* (Imperial College Press, London, 2002).

20. H. H. Hu, N. A. Patankar, and M. Y. Zhu, Direct numerical simulations of fluid-solid systems using the arbitrary Lagrangian-Eulerian technique, *J. Comput. Phys.* **169**, 427–462, (2001).

21. J. A. Sethian and P. Smereka, Level set methods for fluid interfaces, *Ann. Rev. Fluid Mech.* **35**, 341–372, (2003).

22. J. J. Feng, C. Liu, J. Shen, and P. Yue. An energetic variational formulation with phase field methods for interfacial dynamics of complex fluids: advantages and challenges. In eds. M.-C. T. Calderer and E. M. Terentjev, *Modeling of Soft Matter*, pp. pp. 1–26. Springer, New York, (2005).

23. J. W. Cahn and J. E. Hilliard, Free energy of a nonuniform system. I. interfacial free energy, *J. Chem. Phys.* **28**, 258–267, (1958).

24. J. W. Cahn and J. E. Hilliard, Free energy of a nonuniform system. III. nucleation in a two-component incompressible fluid, *J. Chem. Phys.* **31**,

688–699, (1959).

25. P. Yue, J. J. Feng, C. Liu, and J. Shen, A diffuse-interface method for simulating two-phase flows of complex fluids, *J. Fluid Mech.* **515**, 293–317, (2004).

26. P. Yue, C. Zhou, J. J. Feng, C. F. Ollivier-Gooch, and H. H. Hu, Phase-field simulations of interfacial dynamics in viscoelastic fluids using finite elements with adaptive meshing, *J. Comput. Phys.* **219**, 47–67, (2006).

27. C. Zhou, P. Yue, J. J. Feng, C. F. Ollivier-Gooch, and H. H. Hu, 3D phase-field simulations of interfacial dynamics in Newtonian and viscoelastic fluids, *J. Comput. Phys.* **229**, 498–511, (2010).

28. P. Yue, C. Zhou, and J. J. Feng, A computational study of the coalescence between a drop and an interface in Newtonian and viscoelastic fluids, *Phys. Fluids.* **18**, 102102, (2006).

29. P. Poulin, H. Stark, T. C. Lubensky, and D. A. Weitz, Novel colloidal interactions in anisotropic fluids, *Science.* **275**, 1770–1773, (1997).

30. J. C. Loudet, P. Barois, and P. Poulin, Colloidal ordering from phase separation in a liquid crystalline continuous phase, *Nature.* **407**, 611–613, (2000).

31. I. Musevic, M. Skarabot, U. Tkalec, M. Ravnik, and S. Zumer, Two-dimensional nematic colloidal crystals self-assembled by topological defects, *Science.* **313**, 954–958, (2006).

32. P. G. de Gennes and J. Prost, *The Physics of Liquid Crystals.* (Oxford, New York, 1993).

33. E. M. Terentjev, Disclination loops, standing alone and around solid particles, in nematic liquid crystals, *Phys. Rev. E.* **51**, 1330–1337, (1995).

34. T. C. Lubensky, D. Pettey, N. Currier, and H. Stark, Topological defects and interactions in nematic emulsions, *Phys. Rev. E.* **57**, 610–625, (1998).

35. J. J. Feng and C. Zhou, Orientational defects near colloidal particles in a nematic liquid crystal, *J. Colloid Interface Sci.* **269**, 72–78, (2004).

36. Y. Gu and N. L. Abbott, Observation of Saturn-ring defects around solid microspheres in nematic liquid crystals, *Phys. Rev. Lett.* **85**, 4719–4722, (2000).

37. S. Khullar, C. Zhou, and J. J. Feng, Dynamic evolution of topological defects around drops and bubbles rising in a nematic liquid crystal, *Phys. Rev. Lett.* **99**, 237802, (2007).

38. C. Zhou, P. Yue, and J. J. Feng, The rise of Newtonian drops in a nematic liquid crystal, *J. Fluid Mech.* **593**, 385–404, (2007).

39. C. Zhou, P. Yue, and J. J. Feng, Dynamic simulation of droplet interaction and self-assembly in a nematic liquid crystal, *Langmuir.* **24**, 3099–3110, (2008).

40. F. M. Leslie, Some constitutive equations for liquid crystals, *Arch. Rational Mech. Anal.* **28**, 265–283, (1968).

41. P. Poulin, V. Cabuil, and D. A. Weitz, Direct measurement of colloidal forces in an anisotropic solvent, *Phys. Rev. Lett.* **79**, 4862–4865, (1997).

42. C. M. Noël, G. Bossis, A.-M. Chaze, F. Giulieri, and S. Lacis, Measurement of elastic forces between iron colloidal particles in a nematic liquid crystal, *Phys. Rev. Lett.* **96**, 217801, (2006).